THE ASTROPHYSICAL JOURNAL, 422:126–135, 1994 February 10

ELEMENTAL ABUNDANCES OF THE SUPERNOVA REMNANT G292.0+1.8: EVIDENCE FOR A MASSIVE PROGENITOR

JOHN P. HUGHES[1]
Harvard-Smithsonian Center for Astrophysics, 60 Garden Street, Cambridge, MA 02138; and Department of Physics, Kyoto University
AND
K. P. SINGH[2]
Tata Institute of Fundamental Research, Homi Bhabha Road, Bombay, 400 005 India
Received 1993 May 17; accepted 1993 August 17

ABSTRACT

We present a comprehensive nonequilibrium ionization (NEI) analysis of X-ray spectral data from the *Einstein Observatory* and *EXOSAT* for the supernova remnant G292.0+1.8. The spectra are well described by a single-temperature, single-timescale NEI model with $kT = 1.64^{+0.29}_{-0.19}$ keV and $n_e t = (5.55^{+1.20}_{-1.12}) \times 10^{10}$ cm^{-3} s, which establishes that this remnant is indeed young and in the ionizing phase of evolution of its X-ray spectrum. We determine the abundances of the elements O, Ne, Mg, Si, S, Ar, and Fe and examine their variation over the allowed range of column density, kT, and $n_e t$. Numerical calculations of the nucleosynthesis expected for a 25 $M_\odot$ progenitor agree best with the fitted abundances; in fact the minimum rms percent difference between this model and the derived abundances is only 15%. From the fitted emission measure and a simple geometric model of the remnant we estimate the mass of X-ray–emitting plasma to be $9.3^{+11.9}_{-6.2}$ $M_\odot$, for an assumed distance of 4.8 ± 1.6 kpc. Additional errors on this mass estimate, from clumping of the ejecta, for example, may be substantial. No evidence was found for a difference in the thermodynamic state of the plasma as a function of elemental composition based on analysis of the individual ionization timescales of the various species. In this sense then, G292.0+1.8 resembles the remnant Cas A (another product of a massive star supernova), while it is different from the remnants of SN 1572 (Tycho) and SN 1006, both of which are believed to be from Type Ia supernovae.

Subject headings: ISM: abundances — ISM: individual (G292.0+1.8) — nuclear reactions, nucleosynthesis, abundances — supernova remnants — X-rays: interstellar

1. INTRODUCTION

Supernovae (SNs) and their remnants are the key to our understanding of the origin of the chemical elements in the universe. SN explosions not only modify the products of nuclear burning during the hydrostatic evolution of the precursor but also disperse those products, the SN ejecta, into the surrounding interstellar medium (ISM), thereby serving as the principal contributor to the chemical evolution of galaxies. For a number of years now, researchers have been developing detailed numerical models for nucleosynthesis in both massive stars and during the deflagration of a carbon-oxygen white dwarf (see the recent review by Thielemann, Nomoto, & Hashimoto 1990). These two classes of objects are believed to be the progenitors of most types of SN explosions. Models for the nucleosynthetic yield as a function of stellar mass have been extremely useful in the study of the metal enrichment of the gas in systems ranging from our Galaxy (Thielemann et al. 1990) and other nearby systems (Wang & Silk 1993) to clusters of galaxies (Arnaud et al. 1992). On the other hand, support for these models from actual fits to abundance distributions for individual SNs or supernova remnants (SNRs) has been much more limited. The accurate determination of the mass of nickel ejected in the explosion of SN 1987A through study of its light curve and gamma-ray lines is one dramatic exception (Arnett et al. 1989).

Observations of young SNRs in the X-ray band have the potential to provide extremely valuable constraints on the nucleosynthesis models. One reason is that the dominant emission mechanism for the shock-heated gas in young SNRs is thermal bremsstrahlung with a characteristic temperature of several tens of million degrees kelvin. At these temperatures, one can observe in the X-ray band strong line emission from highly ionized atoms of the elements from oxygen to iron from which relative abundance information may be derived. Tempering this potential, however, has been a basic inherent complexity to the interpretation of SNR X-ray spectra; namely, the fact that the dynamical timescale for remnant evolution is less than (and often considerably less than) the timescales for some of the atomic processes which give rise to the observed X-ray emission. In particular, the ionization state of the hot plasma in young SNRs is observed to lag behind the equilibrium state. This nonequilibrium ionization (NEI) effect can influence strongly the emergent X-ray line emission and must be accounted for in order to derive reliable abundance information from X-ray spectral data.

Most previous studies of supernova remnant X-ray spectra which incorporated NEI effects (Itoh 1977; Gronenschild & Mewe 1982; Shull 1982; Hamilton, Sarazin, & Chevalier 1983; Nugent et al. 1984; and Hughes & Helfand 1985) coupled the ionization calculation to detailed models, either analytical or numerical, for the temperature and density evolution of the hot gas in SNRs. In the present work we use a considerably simpler NEI model in which the thermodynamic state of the plasma is characterized by mean values for the ionization timescale and temperature. One advantage of this model is its ease of calculation which makes it possible to explore a broad range of the parameters in direct fits to data. Recently this model has been

[1] E-mail: jph@cfa.harvard.edu.
[2] E-mail: singh@tifrvax.tifr.res.in.

applied successfully to X-ray data on the SNR N132D in the Large Magellanic Cloud (LMC) (Hwang et al. 1993) and the Galactic remnant W44 (Harrus, Hughes, & Singh 1994). In this article we discuss our analysis of archival X-ray data for the SNR G292.0+1.8.

G292.0+1.8 (MSH 11-54) is among the brightest SNRs discovered in the early radio surveys of the southern sky (Milne 1969; Shaver & Goss 1970). Subsequent radio observations by Lockhart et al. (1977) and by Braun et al. (1986) revealed its radio structure to consist of a strong central source of $\sim 2'$ diameter and an extended faint region or a plateau of $\sim 10'$ diameter around the center, but no shell-like structure was seen. Its radio spectrum is intermediate between that of a typical shell-type remnant and a Crab-type remnant (Goss et al. 1979). In the optical band, the spectrum is dominated by oxygen and neon emission lines (Goss et al. 1979; Murdin & Clark 1979). It, therefore, belongs to a class of oxygen-rich SNRs, typical examples of which are Cassiopeia A, Puppis A, and N132D. Murdin & Clark (1979) reported high-velocity ~ 2000 km s^{-1} oxygen- and neon-emitting filaments near the center of the remnant, with low-velocity material of more normal composition being uniformly spread throughout. They suggest that G292.0+1.8 is a young SNR (with an age < 1600 yr) in which the supernova ejecta has not yet fully mixed with the swept-up circumstellar material (CSM).

The X-ray emission from G292.0+1.8 was first reported by Share et al. (1978) in the 1–10 keV band and later confirmed by Agrawal & Riegler (1980) in the 0.5–2.0 keV. A high-resolution X-ray image of the remnant, taken by the *Einstein* high-resolution imager (HRI), revealed a peculiar X-ray morphology: a central barlike structure superposed on an ellipsoidal "disk" of nearly uniform surface brightness (Tuohy, Clark, & Burton 1982). X-ray spectral observations with the *Einstein* solid state spectrometer (SSS) (Clark, Tuohy, & Becker 1980) showed strong line emission from highly ionized magnesium, silicon, and sulfur atoms. These data were analyzed in the usual fashion for that era, using two-temperature collisional ionization equilibrium (CIE) plasma models (e.g., Raymond & Smith 1977). Near-solar values for the abundance of magnesium and silicon but a relative overabundance of sulfur were the principal derived results. Additional X-ray observations were made with the *Einstein* imaging proportional counter (IPC) over the band 0.5–4 keV and the *EXOSAT* medium energy detectors (ME) over the band 1–10 keV. The *EXOSAT* data were analyzed using two-temperature CIE plasma models, and temperatures of 0.5 keV and 2.0 keV were found (Claas 1988). This study also found evidence for a difference between the X-ray spectra of the bar versus disk region based on analysis of images taken by the low-energy (LE) telescope on *EXOSAT* through different filters.

Each of these data sets has limitations (e.g., the narrow bandwidth of the SSS and the coarse spectral resolution of the ME) which make separate detailed spectral analysis difficult. However, joint spectral analysis can overcome these limitations to some extent. In this paper we have carried out simultaneous fits to the IPC, SSS, and ME data so as to cover the broadest possible energy range, roughly 0.5–10 keV. We first checked the consistency of the different data sets by fitting simple analytic models for the continuum (exponential plus Gaunt factor) and line emission (Gaussian profiles). Then the NEI plasma emissivity model was fitted.

The NEI model was used to probe the thermodynamic state of the plasma. In particular the following questions were addressed: (1) Does a single-temperature, single-timescale NEI model adequately describe the current data sets? (2) What are the differences (if any) among the thermodynamic states derived for the various elemental species? (3) Are the derived abundances consistent with the nucleosynthesis models? In producing answers to these questions, we have learned about the nature of the progenitor to G292.0+1.8 and have gained insight into the workings of supernova explosions.

The paper is organized as follows. In § 2 we describe the data. In § 3 we describe the analysis and results from fits to the NEI model, and in § 4 we discuss the implications of our results regarding the progenitor of G292.0+1.8 and compare our results with models of expected yields from nucleosynthesis in massive stars. We also place our results for G292.0+1.8 in the context of results for other young SNRs. Finally § 5 summarizes.

2. DATA

2.1. *EXOSAT ME*

The *EXOSAT* ME detectors were nonimaging gas-filled proportional counters with a field of view of approximately 45′ (FWHM). From the *EXOSAT* database, we obtained the data from the argon-filled detectors which were sensitive in the range of 1–10 keV. Further technical details of the ME detectors are given in Turner, Smith, & Zimmermann (1981). G292+1.8 was viewed 4 times during 1984 and 1985 by *EXOSAT*. We examined the data from each of these observations individually and selected the data with the best background subtraction and the highest available quality flag ($QF = 3$). The data that qualified these criteria belong to observations carried out on 1984 February 22 and 1985 January 19 with a total useful exposure of 45,760 s. Due to the possibility of gain drift between the two sets of observations, we generated separate response matrices for the two observations using the appropriate gain parameters. In preliminary fits it was found that these data sets were consistent with each other, and so we averaged the data and the response functions (weighting them by exposure time).

2.2. *SSS*

The *Einstein* SSS was a cryogenic Si (Li) detector with an energy resolution of about 160 eV (FWHM) over the 0.6–4.5 keV band (Giacconi et al. 1979). Its field of view was roughly 3′ in radius. The SSS observation of G292.0+1.8 took place on 1979 February 1, and useful data were obtained for an exposure time of 6226 s. These data were previously described by Clark et al. (1980). We obtained the data and appropriate response function from the *EXOSAT* database and integrated them into our own spectral fitting code. Our data extraction and analysis procedures were verified by analyzing the SSS data on the Crab Nebula as described in Hwang et al. (1993).

One recent new feature of SSS data analysis has been the development of a model to account for the problem of ice formation on the detector window (N. White and the NASA HEASARC, private communication) which has made possible analysis of SSS data to lower energies than previously. The transmission through the ice layer estimated from the model for the observation of G292.0+1.8 is $0.071^{+0.117}_{-0.046}$ at 0.6 keV. Our results from spectral fitting using the nominal ice layer thickness (see below) give an inferred transmission through the interstellar medium of $0.0025^{+0.0085}_{-0.0010}$, also at 0.6 keV. At the best-fit value the absorption due to the ice layer clearly is

dominated by the ISM column. The fact that our derived column densities are consistent with reddening estimates from optical studies (Braun et al. 1986) makes us confident in the use of the nominal parameters for the ice model. Nevertheless, in the following it should be remembered that some of the uncertainty in the derived column density to G292.0+1.8 may be due to the uncertainty in the model for the transmission through the ice.

We did note one peculiarity with the revised effective area calibration of the SSS. In our initial comparison of the energy centroids for the magnesium, silicon, and sulfur Kα line complexes, we found that when the modeled magnesium and sulfur line energies were well matched to the data, the modeled silicon lines were systematically displaced to higher energies compared to the data. Indeed, the inferred ionization timescale for the silicon lines was over an order of magnitude less than the inferred timescale from the other two elements. We believe this has an instrumental origin. First we note that the nominal SSS spectral model energy binning of constant 36 eV wide bins is probably too coarse for precise modeling of the silicon lines from astrophysical sources for the following reason. The single energy bin spanning the range from 1.8253 to 1.8613 keV contains two of the lines from the helium-like triplet, the Kα lines from Li-like and Be-like silicon, and, most important for a detector composed of silicon (like the SSS), the K-edge of neutral silicon. Such edges are notoriously difficult to model. In addition, the SSS effective area values were adjusted to obtain an acceptable fit to a continuum source (the Crab Nebula), a procedure which does not necessarily account properly for sharp features in the instrumental response. In summary we feel that the current SSS response does not adequately describe the energy region near the K-edge of neutral silicon. As an ad hoc fix to this problem, we artificially adjusted the lower energy of the SSS model bin mentioned above until we obtained reasonable agreement among the ionization timescales of magnesium, silicon, and sulfur. An increase in the energy of the bin of 18 eV was required. In future astrophysics missions with silicon-based detectors, such as *ASCA* (*ASTRO D*) and AXAF-I, appropriate attention must be paid to the complexity of the instrumental response in the energy band around 1.839 keV.

2.3. *IPC*

The IPC was basically an imaging instrument with a 1° field of view and ~1′ spatial resolution (Giacconi et al. 1979). It did, however, provide moderate energy resolution ($E/\Delta E \sim 1$ at 1 keV) over the low-energy X-ray band (0.2–4.5 keV). The IPC observed G292.0+1.8 on 1979 July 11 for a (dead-time–corrected) exposure time of 1780.2 s. The resultant X-ray image is given in Seward (1990). Although the remnant is clearly extended, about 4′ in radius, this size is still too small for spatially resolved spectroscopy with the IPC. We present here for the first time an analysis of the integrated IPC spectrum of G292.0+1.8.

The data were extracted from within a radius of 5′ from the center of the SNR. Background was subtracted from a gain-matched field (sequence I3670), and in each pulse-height channel a 20% uncertainty in background rate was included in quadrature with the statistical error. We included an additional systematic error of 3% to account for temporal and spatial variations in the IPC gain parameters. In our fits we explored the effects of varying the gain parameters and increasing the radius from which the data were extracted (to 10′). None of these introduced significant changes in the fitted results.

2.4. *Consistency among Data Sets*

The data were analyzed first to study the consistency of the spectral data from the various instruments. We used bremsstrahlung emission, including the temperature-dependent Gaunt factor (Karzas & Latter 1961, as calculated by Kellogg, Baldwin, & Koch 1975) for fitting the continuum and gaussians for fitting the line profiles. This preliminary analysis, apart from providing the consistency check, was also a useful guide to the later analysis using the NEI plasma emissivity model. A single-component bremsstrahlung continuum model (with $kT \sim 1.6$ eV) was able to fit the entire energy band, and there were eight emission lines at energies of 0.93, 1.09, 1.33 (Mg), 1.55, 1.84 (Si), 2.11, 2.45 (S), and 6.68 (Fe) keV which were significant. The χ^2 was 158.5 for 122 degrees of freedom. The identification of elemental species with Kα line is given, when clear. At the low-energy end the lines are more significantly blended and the relationship between fitted line centroid and elemental species is somewhat ambiguous. Information about these elemental species can be obtained in the context of the NEI model as we show in the next section.

During the course of this analysis it became apparent, however, that there would need to be a relative normalization applied to the several data sets to account for differences in the fields of view in comparison to the size of the SNR. Because of its large field of view, the ME observed the entire SNR and so the relative normalizations of the *Einstein* detectors were referenced to it. The SSS was found to require a factor of 0.8 relative normalization, while the IPC required a factor of about 1.5. These values were found both for the parametric fits described above as well as the NEI model to be discussed below. Although the reduced factor for the SSS is due to its field of view being smaller than the size of the remnant, the large factor for the IPC was unanticipated, and we do not have an explanation for it. The discrepancy may indicate that the low-energy spectrum of G292.0+1.8 is more complicated than predicted by our current model. However, the reasonable agreement in overall shape between the IPC spectral data and the model (i.e., the residuals do not increase or decrease systematically with energy) argues somewhat against this explanation. It should also be kept in mind that the relative normalizations of these datasets are uncertain by at least 20% due to residual calibration uncertainties (even between the two *Einstein* instruments; see Hwang et al. 1993) and there is probably another factor of at least 10%–20% due to the size of the remnant, including its grain scattering halo (a common feature for Galactic SNRs; see Mauche & Gorenstein 1989). For the most part our results given below are driven by the SSS and ME data and so even if we completely disregarded the IPC data, our conclusions would not change significantly. Low-energy X-ray observations of the remnant with the *ROSAT* PSPC may help to resolve this discrepancy.

3. NEI ANALYSIS

3.1. *Nonequilibrium Ionization*

It has become clear in recent years that SNRs are not well described by simple models of spherically symmetric evolution into homogeneous media (e.g., Sedov 1959). X-ray imaging data (Seward 1990; Mathewson et al. 1983) show remnants with strong asymmetries, rings, and incomplete shells, expansion into preexisting cavities, strong clumping, and so on. The

X-ray image of G292.0+1.8 certainly shows several of these features. In this situation, then, it does not seem necessarily advantageous (or strictly correct for that matter) to assume a particular form for the dynamical evolution of remnants when calculating NEI plasma emissivity models. We have taken an approach which is free of any assumptions about the dynamical evolution and instead assume that the emergent X-ray spectrum of a SNR may be described by mean values for the global plasma temperature and ionization timescale. This model then represents the logical extension of such well-known and widely used CIE models as those of Raymond & Smith (1977), for example, to the NEI situation.

We implement this NEI model by assuming that a parcel of gas was instantaneously shock-heated to a temperature kT some time ago, t. Once heated the gas remains at constant density n_e, and temperature. The gas that enters the shock is assumed to have the ionization state appropriate to gas in CIE at a temperature of roughly 10^4 K. The ionization proceeds towards the equilibrium state (at the shock temperature) with a characteristic timescale given by the product of the electron density and the time since the shock passed, $n_e t$, the so-called ionization timescale. The values that we derive for these parameters from fits to global X-ray spectra represent time-averaged and emissivity-weighted values for kT and $n_e t$ throughout the remnant. If the data warrant, additional NEI models with different temperatures and timescales may (and should) be included.

Calculation of the nonequilibrium ionization fractions was performed using the matrix diagonizational technique developed by Hughes & Helfand (1985). This calculation was mated to the Raymond & Smith (1977; 1992 July 27 version) plasma emission code from which the ionization and recombination rates were obtained. In addition to the numerous emission lines provided by this code, it was necessary to include a few additional lines, appropriate to the NEI situation, from Mewe, Gronenschild, & van den Oord (1985). Continuum emission from radiative recombination, two-photon, and bremsstrahlung, was also computed for each species. Emission spectra from the astrophysically abundant elements H, He, C, N, O, Ne, Mg, Si, S, Ar, Ca, Fe, and Ni were kept separate so that adjustment of the elemental abundances during fitting could be done. As a verification, we calculated our NEI model in the CIE limit ($n_e t = 3 \times 10^{12}$ cm^{-3} s) for several values of kT spanning the range from 0.1 keV to 10 keV and compared the resulting spectra to those calculated directly from the explicitly CIE model of Raymond & Smith. Although there were some slight differences (at the 10% level or so) in a few line profiles when examined at a spectral resolution similar to that of the SIS on-board *ASCA*, in general the agreement between the NEI model and the explicitly CIE model was excellent. Throughout this article we refer to abundances relative to solar; specifically we employ the values from Raymond & Smith (1977) (in dex) 12.0, 10.93, 8.52, 7.96, 8.82, 7.92, 7.42, 7.52, 7.20, 6.90, 6.30, 7.60, and 6.30 for the above listed elements, respectively. Some more details of the NEI emissivity model and its implementation can be found in § 3.2 of Hwang et al. (1993). Data from Morrison & McCammon (1983) were used to calculate the X-ray absorption due to the line-of-sight ISM column.

3.2. *Single-Temperature, Single-Timescale NEI Models*

A single-temperature, single-timescale NEI model provides an acceptable simultaneous joint fit to the data sets. The IPC, SSS, and ME data with best-fit model are shown in Figure 1, and tabulated values of the fitted parameters are given in Table 1. The errors on N_H, kT, and $n_e t$ are single-parameter 90% confidence level errors ($\chi^2_{min} + 2.71$; Avni 1976; Lampton, Margon, & Bowyer 1976). The error bars on the scaled emission measures of the several species considered are statistical errors at 90% confidence with the global spectral parameters N_H, kT, and $n_e t$ fixed at their best-fit values. Below we show in detail how the various elemental emission measures correlate with variations in these parameters.

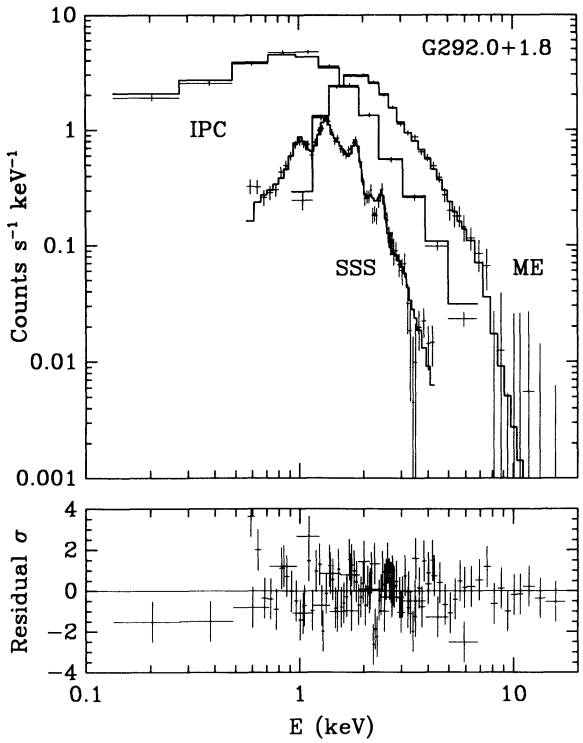

FIG. 1.—The top panel shows the X-ray spectra of G292.0+1.8 from the *Einstein* IPC and SSS and the *EXOSAT* ME with best-fit nonequilibrium ionization model. The residual spectrum (observed data minus best-fit model) is shown in the bottom panel.

TABLE 1

BEST-FIT PARAMETERS FOR NEI MODEL

Parameter	Best-fit Value[a]
N_H (atoms cm^{-2})	$(8.04^{+0.68}_{-1.98}) \times 10^{21}$
kT (keV)	$1.64^{+0.29}_{-0.19}$
$n_e t$ (cm^{-3} s)	$(5.55^{+1.20}_{-1.12}) \times 10^{10}$
$n_H n_e V$[b] (cm^{-3})	$(0.43 \pm 0.37) \times 10^{58}$
$n_O n_e V/[O/H]_\odot$[b] (cm^{-3})	$(22.6^{+2.7}_{-3.2}) \times 10^{58}$
$n_{Ne} n_e V/[Ne/H]_\odot$[b] (cm^{-3})	$(6.4^{+2.7}_{-3.2}) \times 10^{58}$
$n_{Mg} n_e V/[Mg/H]_\odot$[b] (cm^{-3})	$(7.88 \pm 0.40) \times 10^{58}$
$n_{Si} n_e V/[Si/H]_\odot$[b] (cm^{-3})	$(2.14 \pm 0.14) \times 10^{58}$
$n_S n_e V/[S/H]_\odot$[b] (cm^{-3})	$(1.29 \pm 0.24) \times 10^{58}$
$n_{Ar} n_e V/[Ar/H]_\odot$[b] (cm^{-3})	$(0.45^{+0.79}_{-0.45}) \times 10^{58}$
$n_{Fe} n_e V/[Fe/H]_\odot$[b] (cm^{-3})	$(3.0^{+1.1}_{-1.0}) \times 10^{58}$
χ^2 (d.o.f)	154.34 (130)

[a] Statistical errors at 90% confidence.

[b] Emission measure scaled by solar abundance relative to H. Assumes a distance of 4.8 kpc to G292.0+1.8. For the best-fit values of the parameters in the table, $n_e/n_H = 1.47$.

The quoted χ^2 value implies a confidence level for rejection of 92.9%. Breaking the total χ^2 down by instrument we have values of 23.26 (IPC), 85.76 (SSS), and 45.32 (ME) for 12, 80, and 52 data channels, respectively. (Note that the SSS and ME spectra in Fig. 1 were rebinned at the upper energy ends slightly to produce a more pleasing display.) Most of the "extra" χ^2 value is associated with the IPC data, and in fact the IPC residual spectrum shows a characteristic pattern (the data are higher than the model at about 1 keV and vice versa at higher and lower energies), which may indicate residual uncertainties in the effective area or detector gain calibration. In addition to the 11 parameters listed in Table 1, we fitted two relative normalizations (as discussed above) as well as the intensity of a relatively minor background-subtraction correction spectrum for the SSS data. The fitted value for this latter quantity (0.29) was within the range nominally expected.

The value for the ionization timescale $(5.55^{+1.20}_{-1.12}) \times 10^{10}$ cm^{-3} s is quite far from equilibrium (roughly 3×10^{12} cm^{-3} s) and comfortably establishes that this remnant is in the ionizing phase of evolution of its X-ray spectrum. Below we derive values for the plasma density from our spectral fits and a simple geometric model of the SNR which allows us to estimate the remnant's age from the ionization timescale and we find values between 1000 and 3000 yr, fully consistent with the dynamical age estimates from the optical studies of Murdin & Clark (1979). This provides further support for the NEI interpretation of the X-ray spectra. Both the ionization timescale and plasma temperature are consistent with values found for other young remnants such as Cassiopeia A and Tycho (Hughes 1991). The ISM column, $8.04^{+0.68}_{-1.98} \times 10^{21}$ H atoms cm^{-2}, agrees with estimates of the column made by converting optical extinction A_V to N_H using the empirical relationship given by Gorenstein (1975). Murdin & Clark (1979) estimate A_V for G292.0+1.8 in two ways: (1) from the Balmer decrement for low-velocity material, and (2) from the ratios of oxygen lines from the high-velocity material. They find values of 3.8 ± 0.3 and 2 ± 2 for the two cases, respectively, which convert to column densities of $(8.4 \pm 0.7) \times 10^{21}$ H atoms cm^{-2} and $(4.4 \pm 4.4) \times 10^{21}$ H atoms cm^{-2}.

In Table 1 we quote the best-fit emission measures for the elements with strong K-shell line emission in the observed band assuming a distance to the remnant of 4.8 kpc (Saken, Fesen, & Shull 1992). Each elemental emission measure has been scaled by the appropriate solar abundance relative to hydrogen so that for a plasma with solar abundances, the scaled elemental emission measures would all be equal. Thus in order to calculate the absolute abundance of a specific species relative to solar, one merely needs to take the ratio of its scaled emission measure to that of the hydrogen emission measure. We see that, at the best-fit values for G292.0+1.8, the elemental abundances are all greater than solar.

Emission from He, C, and N was included in the fits but with abundances fixed at the solar ratios. (Note that the ionization states of C and N, plus all heavier elements, were calculated in NEI.) Along with H, these elements contribute continuum emission only in the 0.5–10 keV X-ray band, and hence their relative abundances are impossible to disentangle from analysis of the current data. The absolute abundance values (relative to H) which can be derived from the data given in Table 1 are sensitive to the assumption that the abundances of the light elements are in their solar ratios. For example, a nearly equally good fit to the data sets can be had even if any of the light elements, including H, is entirely absent. All that the data require is that some mixture of the light elements provide that fraction of the observed continuum emission which does not come from the heavier elements. Thus the quoted abundance values can all increase or decrease in proportion to the fraction of light element continuum which comes from hydrogen. We hasten to point out, however, that the ratios of the heavy element emission measures, of which our subsequent analysis makes use, are not sensitive to this effect.

In order to reduce the calculational burden, we did not include emission from either Ca or Ni; neither element contributes significantly to the X-ray emission. Even the emission from Ar is rather poorly constrained and is consistent with zero. However the presence of iron in the spectrum is highly significant: the minimum χ^2 value obtained for a fit without any iron emission is 177.65 for 131 d.o.f. The F-test shows that introducing a single additional free parameter (i.e., the iron abundance) is significant at greater than 99.95% confidence.

We checked for the presence of an additional, higher temperature component by including a zero abundance CIE plasma model along with the NEI one. For a fixed 4 keV temperature, the reduction in χ^2 was only 0.65, which is less than 90% significant (for adding one more free parameter). Because of the high intrinsic column toward the remnant, any limits on the presence of additional thermal components with temperatures less than about 0.5 keV are weak and we have not pursued quantitative estimates of these limits. In the remainder of the article (with one obvious exception near the end of § 4.2) we quote results for the single temperature model.

As mentioned above, the relative elemental abundances are quite sensitive to the values of the global spectral parameters. Figure 2 presents these correlations graphically. The set of three panels at the top shows the variation of χ^2 with the independent variation of each of the global spectral parameters, N_H, kT, and $n_e t$. The horizontal dashed curves in each panel show the χ^2 value used to obtain the 90% confidence level error bounds for three interesting parameters ($\Delta\chi^2 = 6.25$). The bottom three panels show how the derived elemental emission measures vary within these error bounds for each spectral parameter. The dominant effect is that due to the ISM column density. For several elemental species, the systematic variation of emission measure with column density is much greater than the statistical error (drawn as the error bars on the individual curves). An increase in column density has a particularly strong effect on the derived emission measures of oxygen and iron, since the line emission from these elements occurs at 1 keV or less where the column has its strongest effect. We also point out the rapid decrease in the emission measure of hydrogen as the column density increases. For the largest allowed columns, the continuum emission is being provided almost entirely by oxygen atoms and there is no "room" left in the fits for emission from the light elements. Interpretation of the elemental abundances in the context of nucleosynthesis models must take account of these correlations. We do so in § 4 below.

3.3. *Ionization Timescales for Different Elements*

Of great interest for research into the nature of supernovae and their remnants concerns the issue of large-scale, radial mixing in the SN ejecta. Our best evidence for such mixing comes from studies of the Type II SN 1987A in the LMC. These lines of evidence include the early appearance of soft X-rays and γ-rays as well as fits to the bolometric light curves (see numerous references in Woosley 1991a). It is believed that

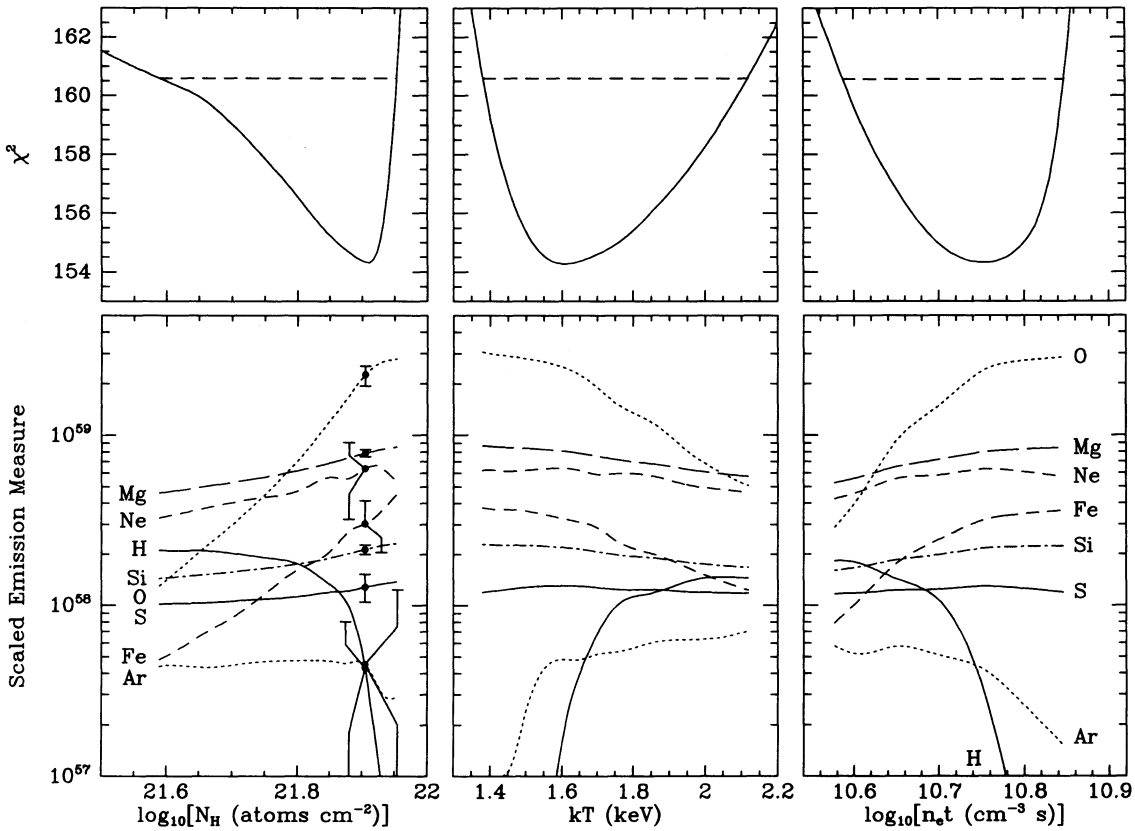

FIG. 2.—The effect of variation in column density (N_H), temperature (kT), and ionization timescale ($n_e t$) on the best-fit emission measures of the various species considered from fits to the G292.0+1.8 X-ray spectra using the nonequilibrium ionization model. The top three panels show the change in χ^2 with the independent variation of each spectral parameter. The 90% confidence interval (for three interesting parameters) is shown in each panel as a dashed line ($\chi^2_{min} + 6.25$). The variations of elemental emission measures (scaled by the appropriate solar abundance value relative to H) are shown in the bottom panels. The error bars are plotted at the best-fit values and represent the statistical error at 90% confidence.

a significant amount of newly synthesized nickel was mixed from the core of the SN out to the parts of the ejecta containing lighter elements and vice versa. Evidence for mixing in other SNs is less well established. Branch et al. (1985) required mixing in the outer half of a Type Ia SN (SN 1981B) to explain the early-time optical spectrum. In this case mixing was required to produce the observed velocity broadening of several Si, S, Ca, and Co lines and to match their blueshifts and absorption depths. However, only a small fraction (about 16% by mass) of the total iron-peak elements were mixed to higher velocities; the bulk of the core was left undisturbed.

X-ray observations of SNRs have the potential to shed light on the issue of just how common mixing is in SNs and whether it happens to a comparable extent for all SN types. In the complete absence of mixing, as the reverse shock passes inward through the ejecta, it progressively shocks material with ever-increasing atomic number until the iron-rich core is reached. One might expect to see a difference, then, in the inferred thermodynamic state of the plasma as a function of elemental species. This would presumably include both differing temperatures and ionization timescales. In the scenario outlined above, matter near the core would tend to have a lower ionization timescale due to (1) the more recent passage of the reverse shock and (2) a lower density in the shocked gas due to adiabatic decompression from the general expansion of the ejecta. In at least one case (Tycho's SNR) a difference of an order of magnitude in the ionization timescale of Fe compared to those from Si, S, Ar, and Ca has been observed, with the Fe timescale being lower than the others (Hughes 1991). Interpretation of possible temperature differences are more complicated, since effects such as electron-ion equipartition at the SN shock fronts are not yet fully understood. Furthermore, varying the ionization timescale from element to element has a more "local" effect on the global X-ray spectrum, since it mostly influences the energy centroid of the Kα line from the particular element considered, than varying the temperature, which would change the shape of the continuum over the whole band. For these reasons we use the ionization timescale to indicate differences in the thermodynamic state of the plasma as a function of elemental species.

We searched for differences in the ionization timescales among the various elements with strong K-shell lines in the G292.0+1.8 data. Our approach was to introduce a separate ionization timescale for one element at a time, while keeping the timescale for the remaining elements tied together. In the fits both timescales were allowed to be free. All other parameters, abundances, column density, etc., were allowed to be free as well, so that in the global fit there was one additional free parameter. The results are shown in Figure 3. The top panel shows the significance level (from the F-test) associated with the inclusion of a separate ionization timescale for the elements shown. No species shows a result significant at even the 2 σ level. The bottom panel quotes the actual individual ionization timescales and their error bars. All are consistent with the

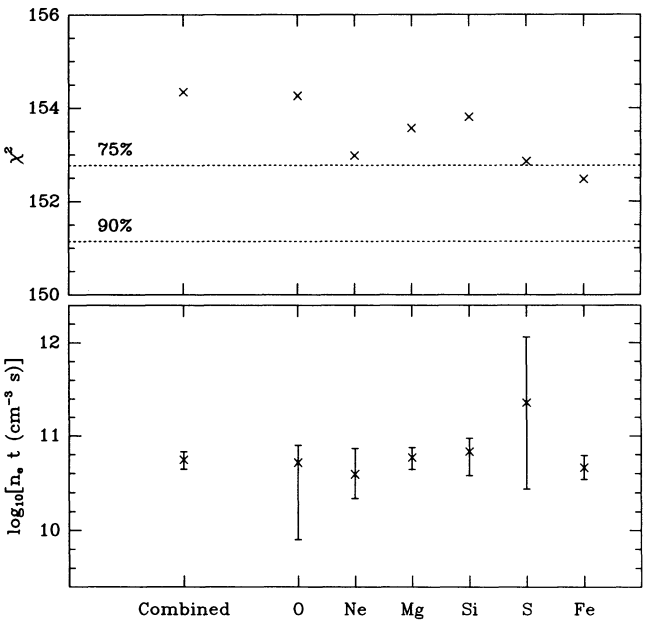

FIG. 3.—The effect of introducing a separate, independent ionization timescale for each of the elemental species listed in the axis label. The top panel shows the best-fit χ^2 values for the several cases. The dashed lines indicate the values of χ^2 at which the introduction of an additional free parameter would be significant at the 75% and 90% confidence levels (from the F-test). In no case is the introduction of an additional free parameter significant. The bottom panel shows the best-fit values (and 90% errors) for the ionization timescales from the various species considered. All values are consistent with a single, combined value.

single, combined value shown on the left-hand-side. The lines from Ne and Mg are among the strongest in the SSS spectrum, and consequently the error bars on their ionization timescales are among the smallest. Although the Si lines are strong, the determination of the Si ionization timescale is severely compromised by the ad hoc correction we were required to apply to the SSS response function, due to its Si-based composition, as discussed above. The limits on the ionization timescale of Fe are rather good since the broad energy band coverage of the joint data sets encompasses both the K- and L-shell emission lines from Fe.

We conclude that there is no evidence for differences in the thermodynamic state of the plasma in G292.0+1.8 as a function of composition. This supports a scenario in which there was significant mixing of the iron-rich core in the ejecta out at least to the silicon-group layer, as in SN 1987A. This is not to suggest, however, that the ejecta are smooth and homogeneous; the optical and X-ray imaging data both indicate the presence of a significant amount of clumping. Rather, we propose that clumps, which may be of differing elemental composition, are well mixed in the remnant and that those various regions have undergone roughly similar thermal histories regardless of their composition. A useful corollary to this conclusion is that the relative abundances we measure in the SNR from the X-ray data should represent the overall abundance distribution ejected during the SN explosion (with the possible exception of Fe). This is an important point since it allows us to proceed in our comparison of our derived abundances to those from nucleosynthesis models, as we do immediately below.

4. DISCUSSION

4.1. *Comparison to Nucleosynthesis Models*

In their calculations of nucleosynthesis in Type II SNs, Thielemann et al. (1990) artificially induce a shock wave with energy 10^{51} ergs in stars of various mass and follow the explosive burning processes. They use precollapse stellar models calculated by Nomoto & Hashimoto (1988), which include the important effects of nucleosynthesis during the hydrostatic evolution of the progenitor. This source is found to be a significant contributor to the abundances of the lighter elements (up to phosphorus), while nearly all heavier elements are produced during the SN explosion. One particular shortcoming of the technique of using initiated shock waves for these studies is that it is not possible to predict the boundary between the neutron star and the ejecta. Only in the case of SN 1987A was it possible to "calibrate" the location of the so-called mass cut since the amount of radioactive ^{56}Ni ejected in this situation was determined by requiring that it power the light curve. Indirect techniques have been used (Thielemann et al. 1990) to estimate the location of the mass cut in stars with masses different from that of the progenitor of SN 1987A. For this reason then, the predicted amount of Fe ejected from these models of Type II SNs is rather uncertain. This also means that the abundance ratio of oxygen-group to iron-group elements is not a particularly good indicator of progenitor mass. Rather, a more sensitive determination can be done by comparing the abundances of the oxygen group to those of sulfur and the elements beyond (such as Ar and Ca). The oxygen-group elements are produced mostly during hydrostatic burning processes and thus are very sensitive to the progenitor mass, while the higher Z elements are produced explosively and do not vary much as a function of the progenitor mass.

We compared our derived abundances for the elements O, Ne, Mg, Si, S, and Ar with predictions for the 13 $M_\odot$, 15 $M_\odot$, 20 $M_\odot$, and 25 $M_\odot$ progenitors of Thielemann et al. (1990) and a preliminary 40 $M_\odot$ model (F. Thielemann, private communication). We assumed a pure ejecta component; there was no swept-up circumstellar or interstellar matter. The comparison was done as a function of the ISM absorbing column density to the SNR in order to take proper account of the strong correlations among the various elemental species as shown in Figure 2. We opted to compare the model and data in terms of fractional (or percentage) difference, since the dominant source of error is computational and not the statistical errors on the fitted abundances. Figure 4 presents the results for the five progenitor masses as labeled. The curves are drawn only over the 90% confidence range in column density, and the vertical lines show the 68% confidence range. The best fit overall is for the 25 $M_\odot$ progenitor with a minimum rms difference of 15%. One can convert the ordinate axis to an approximate χ^2 value using $\chi^2 \approx 6(\mathrm{rms}/30)^2$, which assumes a 30% error on the model bulk composition values as suggested by Thielemann et al. (1990). Thus models with rms percentage differences greater than about 30.6% can be rejected at 90% confidence ($\chi^2 = 6.25$ for three degrees of freedom). This confidently eliminates the three models near the top of the figure.

For the 25 $M_\odot$ minimum rms case, the amount of Fe derived from the fits is about a factor of 3 more than the amount which Thielemann et al. estimate should be ejected. This might indicate that the location of the mass cut in the models should be revised in order to eject more iron. It is also possible that there is an additional reservoir of unshocked Fe still inside the

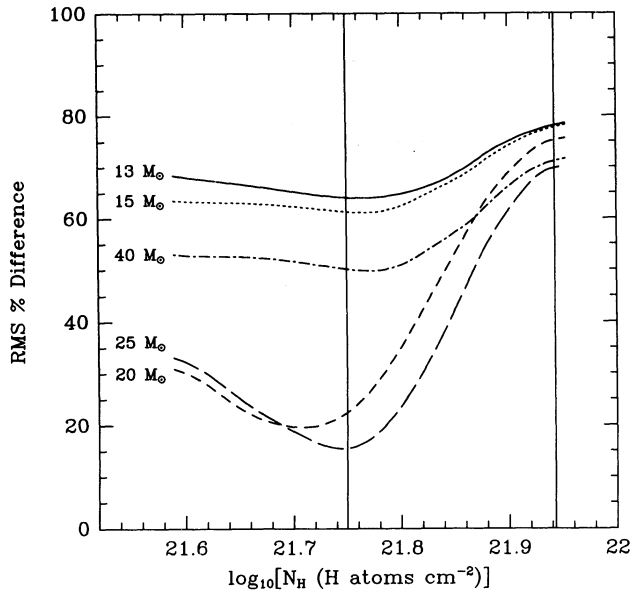

FIG. 4.—Comparison of the derived abundances for the elements oxygen, neon, magnesium, silicon, sulfur, and argon with model predictions for nucleosynthesis in massive stars (Thielemann et al. 1990). The comparison is made in terms of the root mean square (rms) percent difference for the abundance values derived as a function of column density. The curves are plotted only for those values of column density within the 90% confidence level, while the vertical lines show the 68% confidence level range. The minimum rms percent difference is 15% obtained for the 25 $M_\odot$ progenitor model.

present position of the reverse shock in G292.0+1.8. Future higher spectral resolution broad-band X-ray observations may be able to find evidence for this through a more detailed study of the high energy Fe lines.

Finally, we comment on recent nucleosynthesis models from Woosley (1991b) and Weaver & Woosley (1992). The 18 $M_\odot$ and 20 $M_\odot$ (from the former reference) and the 15 $M_\odot$, 25 $M_\odot$, and 35 $M_\odot$ models (from the latter reference) were all much poorer fits to the G292.0+1.8 derived abundances than those of Thielemann et al. The minimum rms percentage difference was no less than 50% for any of the various models over the 90% confidence range in column density. In general, these models tended to overproduce S and Ar, while Ne and Mg were significantly underproduced (for the same level of oxygen production). For example, when the amount of ejected oxygen was normalized between the two models for the 20 $M_\odot$ progenitor, Woosley's models then predicted roughly half as much Ne and Mg and twice as much S and Ar as Thielemann et al. did. The discrepancy was even greater for the 25 $M_\odot$ case: Ne and Mg were only 0.2 of the Thielemann et al. values while S and Ar were over 5 times more abundant. Thielemann et al. (1991) have already noted these differences (at least for the 20 $M_\odot$ case) and attribute it to differences in the structure and composition of the presupernova model. It apparently indicates that the abundance uncertainties in the models are probably larger than the 30% errors quoted above. On the positive side, though, the X-ray data and NEI models may have reached a point where they can help constrain some of the major unknowns in the nucleosynthesis models for massive stars, such as the $^{12}C(\alpha, \gamma)^{16}O$ rate and the role of semiconvective mixing during the hydrostatic evolution of the progenitor.

4.2. *Remnant Mass*

In order to estimate the mass of the X-ray–emitting plasma in G292.0+1.8 we need (1) a spectral model to relate the observed X-ray emissivity to the volume emission measure and (2) a model for the geometry of the remnant. Our NEI model provides the first part. In this section we develop a simple geometric model based on the *Einstein* HRI data for the second.

We have already mentioned the two components to the X-ray image: the central bar and the uniform disk. The bar is reminiscent of a ring seen nearly edge-on; we model it as such and estimate the ring diameter to be roughly 6.6 and its thickness to be about 0.7. For the disk we assume a spherical volume with a diameter of 6.6. We quote volume filling factors for each component, f_R and f_S, to account for both macroscopic factors, such as the thickness of the shell comprising the disk component, and smaller scale-size clumping. From considerations of the macroscopic factors alone, f_S can take on values from 1 for a filled spherical volume to 0.25 for a shell with a thickness 1/12 its radius. Because the emission from the disk is rather uniform and not limb-brightened, it is unlikely that f_S is much less than about 0.5. If the ejecta are strongly clumped, then the f factors could be considerably smaller. With these inputs we obtain the following total volumes for the two components: $V_R = 6.38 \times 10^{56} f_R D^3_{4.8\,\mathrm{kpc}}$ cm^3 and $V_S = 1.20 \times 10^{58} f_S D^3_{4.8\,\mathrm{kpc}}$ cm^3, where $D_{4.8\,\mathrm{kpc}}$ is the distance to the remnant, normalized to 4.8 kpc.

The two components, bar and disk, contribute roughly 30% and 70%, respectively, to the total number of observed counts from the remnant in the HRI image. We use this ratio to apportion the derived emission measures from the NEI fits between the components. Then one can easily derive for the root mean square hydrogen number densities

$$n_R = 1.18^{+1.72}_{-1.02} f_R^{-1/2} D^{-1/2}_{4.8\,\mathrm{kpc}}\ \mathrm{cm}^{-3}$$

and

$$n_S = 0.41^{+0.61}_{-0.36} f_S^{-1/2} D^{-1/2}_{4.8\,\mathrm{kpc}}\ \mathrm{cm}^{-3}\ ,$$

where the errors include the allowed variation of the fitted hydrogen emission measure as shown in Figure 2. In deriving these values we have also used the ratio of electron to hydrogen number density, n_e/n_H, which tends to increase as the metal abundance increases. Values range from a low of 1.18 (for the minimum allowed value of column density) to a high of 6.17 (for the maximum allowed value of column density). For the total masses we obtain

$$M_R = 1.23^{+0.87}_{-0.27} f_R^{1/2} D^{5/2}_{4.8\,\mathrm{kpc}}\ M_\odot$$

and

$$M_S = 8.1^{+5.8}_{-1.7} f_S^{1/2} D^{5/2}_{4.8\,\mathrm{kpc}}\ M_\odot\ .$$

These estimates include the mass in metals as well as H and He. The larger mass estimates arise from those fits which yielded significant values for the hydrogen emission measure, as in the lower allowed range on the column density (see Fig. 2). This material is dominated by hydrogen. The smaller mass estimates arise from the opposite case, where the hydrogen emission measure has become negligible as in the upper end of the column density range. Here nearly 90% of the mass is provided by metals ($Z > 2$).

In a similar manner the thermal energy content in the gas is determined to be $U_R = (0.076^{+0.089}_{-0.046}) \times 10^{50} f_R^{1/2} D^{5/2}_{4.8\,\mathrm{kpc}}$ ergs

and $U_S = (0.51^{+0.58}_{-0.31}) \times 10^{50} f_S^{1/2} D_{4.8\,\mathrm{kpc}}^{5/2}$ ergs. This explicitly assumes that the electron and ion temperatures in the SNR are equal.

The uncertainty on the distance is roughly ± 1.6 kpc (Braun et al. 1986; Saken et al. 1992). Thus we estimate the total mass of X-ray emitting plasma in G292.0+1.8 to be $9.3^{+11.9}_{-6.2}\ M_\odot$. Although additional uncertainties in this estimate due to the simplicity of the geometric model may be substantial, this large a value for the amount of hot plasma in the remnant provides encouraging support for a massive progenitor. And since it is unlikely that the entire mass of ejecta has been thermalized to X-ray temperatures because of the currently low value for the thermal energy content of the gas and the optical observation of high-velocity ejecta in the SNR, sizable amounts of unseen ejecta are almost certainly present as well. A census of material in G292.0+1.8 would not be complete without mentioning the $\sim 1.4\ M_\odot$ of infrared-emitting dust found by Saken et al. (1992) from analysis of *IRAS* data.

For remnants in the Sedov phase of evolution, the ratio of total energy (that is thermal plus kinetic) to thermal energy is 1.39 for expansion into a uniform ISM and 2.0 for expansion into a stellar wind density profile ($\rho \sim r^{-2}$) (Cox & Franco 1981). Assuming the latter case, which is probably more appropriate to G292.0+1.8 than the former, we estimate the SN explosion energy to be $(0.12^{+0.18}_{-0.10}) \times 10^{51}$ ergs (after summing the thermal energy content from the two components). However, since G292.0+1.8 is not yet in the Sedov phase of evolution (once again due to the presence of high-velocity ejecta in the remnant), the ratios of total energy to thermal energy given above are underestimates, and the actual SN explosion energy may be considerably larger.

Finally we note that our decomposition of the image into two components suggests that there should be a difference in the X-ray spectra between them, purely from differences in the ionization timescales and temperatures. If we assume pressure equilibrium and equal shock times for the components, then we obtain values for $n_e t$ and kT of 1.02×10^{11} cm^{-3} s and 0.71 keV for the bar and 3.55×10^{10} cm^{-3} s and 2.04 keV for the disk, which, when averaged by the HRI count ratio, yield the best-fit values in Table 1. We fit the spectral data with a two-component NEI model using these parameters and obtained a not substantially worse best-fit χ^2 of 163.0 (after adjustment of the column density, abundances, and relative normalizations) for the same abundance set in the two regions. This indicates that it might be possible to explain the spectral differences between the bar and disk regions seen in the *EXOSAT* LE filter images (Claas 1988) in the context of a two-component NEI model, without requiring different abundances in the two regions. A more refined analysis is beyond the scope of this paper and would best be carried out with spatially resolved X-ray spectra, such as might be obtained from *ROSAT* or *ASCA* (*ASTRO D*).

4.3. *Comparison to Other Young SNRs*

Hughes (1991) has carried out a NEI analysis of the X-ray spectra of three other young SNRs: Cas A, SN 1572 (Tycho), and SN 1006. The principal conclusion of that work was that the putative remnants of Type Ia SN explosions, i.e., Tycho and SN 1006, showed strong evidence for spatial stratification in their elemental composition, while Cas A, the explosion of a massive star, showed no such evidence for stratification. The Tycho and Cas A results were based on determining the energy centroids of the Kα emission lines from Si, S, Ar, Ca, and Fe and inferring the ionization timescales for each from a NEI model. For Tycho, the inferred ionization timescale from Fe was clearly different from that of the Si-group elements. At the best-fit values, the Fe ionization timescale was roughly an order of magnitude less than the mean of the ionization timescales from Si, S, Ar, and Ca. No such difference in ionization timescale with composition was observed for Cas A. The result for SN 1006 was based on the observation that shock-heated Kα oxygen line emission was present in this remnant (Vartanian, Lum, & Ku 1985) but shock-heated emission from Si- and Fe-group elements was absent (see Hamilton, Sarazin, & Szymkowiak 1986). However a significant amount of unshocked high-velocity Fe in the interior of the SNR was known to exist based on observations of broad Fe II lines seen in absorption through the remnant (Wu et al. 1983).

Based on the analyses presented above we conclude that G292.0+1.8 is similar to Cas A in that both are the remnants of massive stars (see Fabian et al. 1980 for the Cas A analysis), and both show no evidence for a significant difference in the inferred ionization timescales with composition. Thus significant amounts of radial mixing must have occurred in the ejecta of these remnants sometime during or after the SN explosion, similar to what was observed for SN 1987A.

5. CONCLUSIONS

In this article we have presented the first comprehensive NEI analysis of the SNR G292.0+1.8, based on archival *Einstein* and *EXOSAT* data. We find that the remnant can be well represented by a simple NEI plasma model which is independent of assumptions about the hydrodynamic evolution of the remnant and instead incorporates mean values for the temperature and ionization timescale. A single-temperature, single-timescale NEI model is an acceptable fit to the data. From the best-fit value of the ionization timescale we establish that the remnant is young and in the ionizing phase of evolution of its global X-ray spectrum. We develop a technique for analyzing the derived abundances which takes account of the strong correlations of abundance with the global spectral parameters, in particular the ISM column density. The abundances compare well with the model predictions of Thielemann et al. (1990) for a 25 $M_\odot$ progenitor. The models of Woosley (1991b) and Weaver & Woosley (1992), which treat the relevant physics of stellar evolution in a somewhat different manner, are in disagreement with the data. A simple geometric model of the SNR, when combined with the specific emissivity from the NEI model, indicates that a significant amount of hot plasma $9.3^{+11.9}_{-6.2}\ M_\odot$ is present in the remnant. Based on the thermal energy content of the hot plasma and the assumptions (both of which tend to underestimate the energy) that (1) the remnant is in the Sedov phase and expanding into a stellar wind-type density profile and (2) the electron and ion temperatures in the remnant are equal, we estimate the SN explosion energy to be $(0.12^{+0.18}_{-0.10}) \times 10^{51}$ ergs.

We have presented evidence here and elsewhere (Hughes 1991) from analysis of the X-ray spectra of four SNRs that there is a difference in the amount of radial mixing which occurs in different types of SNs. The effect we find, that the remnants of massive stars, such as G292.0+1.8 and Cas A, appear to be strongly mixed, is consistent with scenarios established for the recent bright SN 1987A in the LMC. The two remnants believed to be Type Ia events, Tycho and SN 1006, show much less evidence for mixing and thus the spatial strati-

fication of composition in their ejecta has been largely preserved to the present.

These different types of SNs are widely believed to arise from very different progenitors and quite different processes. Type Ia SN explosions arise from the carbon deflagration of a carbon-oxygen white dwarf in which the burning front moves subsonically. At the end of their lives, massive stars undergo core collapse, bounce, and the formation of a supersonic shock wave as they become Type II (or Type Ib) SNs. Mixing and clumping may occur from Rayleigh-Taylor instabilities as the blast wave propagates down the power-law density gradient of the stellar envelope, although other possibilities exist (see numerous references in Woosley 1991a). The information from SNR X-ray spectra that we have presented here is an important input for these models of SN explosions. It is also exciting to speculate that X-ray observations of young SNRs may allow a posteriori typing of SNs from the study of the derived thermodynamic state as a function of elemental composition. We look forward to the X-ray data from the recently launched Japanese satellite *ASCA* which will expand the number of SNRs for which this type of detailed analysis is possible and thereby allow for further tests of these ideas.

This research has made use of data obtained from the *EXOSAT* database, and the High Energy Astrophysics Science Archive Research Center Online Service, provided by the NASA/Goddard Space Flight Center, also provided useful information. J. P. H. acknowledges the hospitality of K. Koyama and the X-ray astronomy group at Kyoto University which made it possible to complete this paper. We thank Friedel Thielemann for useful discussions and for providing us with the results of the 40 $M_\odot$ model, and we thank Stan Woosley for sending us results prior to publication. K. P. S. acknowledges the hospitality of the High Energy Astrophysics Division of the Center for Astrophysics and thanks the Smithsonian Institution for funding his visit to the CfA. This research was supported in part by the National Science Foundation under grant INT-9308299, by NASA under SADAP grant NAG 8-670, and by Smithsonian Institution funds from the International Exchange Program.

REFERENCES

Agrawal, P. C., & Riegler, G. R. 1980, ApJ, 237, L33
Arnaud, M., Rothenflug, R., Boulade, O., Vigroux, L., & Vangioni-Flam, E. 1992, A&A, 254, 49
Arnett, W. D., Bahcall, R. P., Kirshner, R. P., & Woosley, S. E. 1989, ARA&A, 27, 629
Avni, Y. 1976, ApJ, 210, 642
Branch, D., Doggett, J. B., Nomoto, K., & Thielemann, F.-K. 1985, ApJ, 294, 619
Braun, R., Goss, W. M., Caswell, J. L., & Roger, R. S. 1986, A&A, 162, 259
Clark, D. H., Tuohy, I. R., & Becker, R. H. 1980, MNRAS, 193, 129
Claas, J. J. 1988, in Proc. of the Workshop on Supernova Shells and Their Birth Events, ed. W. Kundt (Berlin: Springer-Verlag), 146
Cox, D. P., & Franco, J. 1981, ApJ, 251, 687
Fabian, A. C., Willingale, R., Pye, J. P., Murray, S. S., & Fabbiano, G. 1980, MNRAS, 193, 175
Giacconi, R., et al. 1979, ApJ, 230, 540
Gorenstein, P. 1975, ApJ, 198, 95
Goss, W. M., Shaver, P. A., Zealey, W. J., Murdin, P., & Clark, D. H. 1979, MNRAS, 188, 357
Gronenschild, E. H. B. M., & Mewe, R. 1982, A&AS, 48, 305
Hamilton, A. J. S., Sarazin, C. L., & Chevalier, R. A. 1983, ApJS, 51, 115
Hamilton, A. J. S., Sarazin, C. L., & Szymkowiak, A. E. 1986, ApJ, 300, 698
Harrus, I., Hughes, J. P., & Singh, K. P. 1994, in preparation
Hughes, J. P. 1991, in Supernovae, The Tenth Santa Cruz Summer Workshop in Astronomy and Astrophysics, ed. S. Woosley (Berlin: Springer-Verlag), 661
Hughes, J. P., & Helfand, D. J. 1985, ApJ, 291, 544
Hwang, U., Hughes, J. P., Canizares, C. R., & Markert, T. H. 1993, ApJ, 414, 219
Itoh, H. 1977, PASJ, 29, 813
Karzas, W., & Latter, R. 1961, ApJS, 6, 167
Kellogg, E., Baldwin, J. R., & Koch, D. 1975, ApJ, 199, 299
Lampton, M., Margon, B., & Bowyer, S. 1976, ApJ, 208, 177
Lockhart, I. A., Goss, W. M., Caswell, J. L., & McAdam, W. B. 1977, MNRAS, 179, 147
Mauche, C. W., & Gorenstein, P. 1989, ApJ, 336, 843
Mathewson, D. S., Ford, V. L., Dopita, M. A., Tuohy, I. R., Long, K. S., & Helfand, D. J. 1983, ApJS, 51, 345
Mewe, R., Gronenschild, E. H. B. M., & van den Oord, G. H. J. 1985, A&AS, 62, 197
Milne, D. K. 1969, Australian J. Phys., 22, 613
Morrison, R., & McCammon, D. 1983, ApJ, 270, 119
Murdin, P., & Clark, D. H. 1979, MNRAS, 189, 501
Nomoto, K., & Hashimoto, M. 1988, Phys. Rep., 163, 13
Nugent, J. J., Pravdo, S. H., Garmire, G. P., Becker, R. H., Tuohy, I. R., & Winkler, P. F. 1984, ApJ, 284, 612
Raymond, J. C., & Smith, B. W. 1977, ApJS, 35, 419
Saken, J. M., Fesen, R. A., & Shull, J. M. 1992, ApJS, 81, 715
Sedov, L. I. 1959, Similarity and Dimensional Methods in Mechanics (New York: Academic)
Seward, F. D. 1990, ApJS, 73, 781
Share, G., et al. 1978, IAU Circ., No. 3169
Shaver, P. A., & Goss, W. M. 1970, Australian J. Phys., Astr. Suppl., 14, 133
Shull, J. M. 1982, ApJ, 262, 308
Thielemann, F.-K., Hashimoto, M., & Nomoto, K. 1991, ApJ, 349, 222
Thielemann, F.-K., Nomoto, K., & Hashimoto, M. 1990, in Supernovae, Les Houches, Session LIV 1990, ed. J. Audouze, S. Bludman, R. Mochkovitch, & J. Zinn-Justin, in press
Tuohy, I. R., Clark, D. H., & Burton, W. M. 1982, ApJ, 260, L65
Turner, M. J. L., Smith, A., & Zimmermann, H. U. 1981, Space Sci. Rev., 30, 479
Vartanian, M. H., Lum, K. S. K., & Ku, W. H.-M. 1985, ApJ, 288, L5
Wang, B., & Silk, J. 1993, ApJ, 406, 580
Weaver, T. A., & Woosley, S. E. 1992, preprint
Woosley, S., ed. 1991a, Supernovae, The Tenth Santa Cruz Summer Workshop in Astronomy and Astrophysics (Berlin: Springer-Verlag)
———. 1991b, in Supernovae, The Tenth Santa Cruz Summer Workshop in Astronomy and Astrophysics, ed. S. Woosley (Berlin: Springer-Verlag), 202
Wu, C.-C., Leventhal, M., Sarazin, C. L., & Gull, T. R. 1983, ApJ, 269, L5